Materials & Design 247 (2024) 113433

Contents lists available at ScienceDirect

Materials & Design

journal homepage: www.elsevier.com/locate/matdes

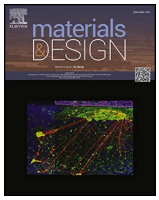

Assessing the fracture toughness in Tungsten-based nanocomposites: A micro-mechanical approach

K. Schmuck, M. Burtscher, M. Alfreider, D. Kiener *

Montanuniversität Leoben, Department of Materials Science, Chair of Materials Physics, Jahnstraße 12, Leoben 8700, Austria

ARTICLE INFO

Keywords:
Tungsten-copper
Tungsten-α-brass
High-pressure torsion
Micro-cantilever bending
Nanocrystalline microstructure

ABSTRACT

Nanocrystalline tungsten-copper composites can favorably combine the outstanding material properties of both elements. This work investigates tungsten-copper composites fabricated from elemental powders with 80 wt.% tungsten and either copper or α-brass containing 20 wt.% zinc, respectively. Moreover, high-pressure torsion is used to compact the powders, strengthen the resulting composite by grain refinement, and tailor the grain-size in the nanocrystalline regime by varying the deformation temperature between RT, 400°C and 550°C, resulting in grain-sizes of 9 nm 14 nm and 28 nm, respectively. Hardness measurements revealed a transition from normal to inverse Hall-Petch behavior for grain-sizes below 11 nm. To examine the fracture properties, micro-cantilever bending beams with a cross-section of 10x10 μm^2 were fabricated. Evaluation of these experiments indicated a fracture toughness of 3 $MPa\sqrt{m}$. The slight decrease of fracture toughness between a grain-size of 9 nm to 14 nm indicates a reduction of the grain boundary cohesion strength. The grain-size increase to 28 nm reversed the trend in fracture toughness and raised it to 3.4 $MPa\sqrt{m}$, which points to activating additional deformation mechanisms, such as dislocation-accumulation and twinning. Additionally, alloying with zinc raised the composites strength and retained the composites fracture toughness, benefiting the damage tolerance.

1. Introduction

Over the last decades, tungsten-copper composites have increasingly attracted the attention of researchers. As the composite allows to inherit the outstanding material properties of both elements, such as high intrinsic strength and hardness at elevated temperatures, ability to withstand high-temperature loads due to a high melting point, good electrical- and thermal conductivity, increased wear and arc erosion resistance, excellent neutron irradiation resistance, low vapor pressure and possible cooling due to transpiration of copper [1–8]. Due to these properties, tungsten-copper composites are commonly used in high-performance applications, in particular for high-voltage switches, electronic packaging, electrodes for resistance welding, aircraft nose cones and military parts [5,6,8–12]. Furthermore, tungsten-copper composites are frequently considered as material candidates for rolling guides in steel production [8] and plasma facing components in fusion reactors [2,4,13–15].

Safety relevant applications require materials that combine high damage- and fracture-tolerance. Both properties can be enhanced by simultaneously increasing the material's strength and ductility, which are naturally mutual exclusive [16–18]. This exclusivity can be mitigated by reducing the grain-size down to the ultra-fine grained and nanocrystalline regime [17,19–21]. Though, in the nanocrystalline regime the strength increase can be reversed below a certain grain-size, known as an inverse Hall-Petch behavior [22–25]. Moreover, by decreasing the grain-size the dominant deformation mechanisms in materials transforms from dislocation mediated to grain boundary governed plasticity. For this transition literature reports a grain-size of about 10 nm and 30 nm for body centered cubic (bcc) and face centered cubic (fcc) materials, respectively [26–28]. Further benefits of refined microstructures arise in applications for plasma facing components, as a finer grain-size shifts the softening effect of irradiation induced helium bubbles to higher doses and inhibits the formation of blisters [16]. Furthermore, Zhang *et al.* [29] reported an increased wear and arc resistance for refined microstructures, benefiting the application in high-voltage contacts.

Still, grain refinement sacrifices ductility due to decreasing strain hardening capabilities, as the accumulation of dislocations is restricted by either the grain-size or dislocation saturation [30–34]. The latter occurs especially for severe plastic deformation techniques due to the

* Corresponding author.
E-mail address: daniel.kiener@unileoben.ac.at (D. Kiener).

https://doi.org/10.1016/j.matdes.2024.113433
Received 25 June 2024; Received in revised form 2 November 2024; Accepted 4 November 2024
Available online 6 November 2024

refinement process and respective saturation. Nevertheless, Zhao *et al.* [33] increased the ductility and strength of high-pressure torsion deformed copper by decreasing the stacking fault energy. The decrease was achieved by alloying copper with zinc, enabling the accumulation of twins as an additional deformation mechanism. To investigate the impact of stacking fault energy to promote the twinning tendency, Zhao *et al.* [34] varied the zinc content of the bulk samples between 0, 10 and 30 wt.%. They concluded that 10 wt.% zinc results in an ideal stacking fault energy, increasing the twinning tendency and enhancing the strain hardening capacities. A similar result was reported by Holub *et al.* [35], using elemental powders as precursors. They alloyed the powders by ball milling, followed by high-pressure torsion compaction of these powders to form bulk samples. These samples were subsequently subjected to further high-pressure torsion (HPT) steps for grain refinement down to the nanocrystalline regime. In addition to the stacking fault energy, the twinning tendency depends also on the grain-size. The ideal grain-size for copper is around 40 nm [36,37].

To the best knowledge of the authors, fracture mechanical studies of nanocrystalline tungsten-copper and tungsten-α-brass composites produced from powders are lacking in the literature. Therefore, this work discusses the fracture mechanics and material parameters for these composites. For that, tungsten-copper and tungsten-α-brass composites with 80 wt.% tungsten were analyzed. A ratio of 90 wt.% copper and 10 wt.% zinc was selected for the α-brass to retrieve an ideal stacking fault energy with a high twinning tendency. This enabled to study the influence of zinc on the different investigated material properties. To obtain a homogeneous microstructure within in the nanocrystalline regime, multiple HPT steps were conducted. Thereby, the temperature of the last deformation step was adjusted to tailor the grain-size. The fracture mechanical response was investigated concerning the microstructural feature size by *in situ* micro-cantilever bending beams.

2. Experimental

2.1. Sample preparation

Due to the lack of available bulk material with the composition of 80 wt.% tungsten, 18 wt.% copper and 2 wt.% zinc, the samples investigated in this study were fabricated from elemental powders: tungsten (2 μm, purity 99.97%, Plansee SE), copper (14–25 μm, purity 99%, Merck KGaA) and zinc (<149 μm, purity 99.9%, Alfa Aesar). The elemental powders were handled in a glove box (M. Braun LABstar Glove Box Workstation) to prevent powder degradation, *e.g.* oxidation.

The copper and zinc powders were mechanically alloyed by ball milling to produce an α-brass powder containing 90 wt.% copper and 10 wt.% zinc. Therefore, the stainless steel vials were filled with 15 g of the powder mixture and 150 g of stainless steel balls with a diameter of 5 mm. Filling and removing the powder from the vials was performed inside the glove box to sustain the argon atmosphere throughout the milling process. The powders were milled in a planetary ball mill (Retsch PM400) for 1.5 h with a periodic sequence of 5 min milling followed by a break of equal duration to reduce a possible thermal influence during milling and to allow vial, grinding medium and powder to cool down [35].

The powders were mixed in the ratio of 80 wt.% tungsten and 20 wt.% of either pure copper or α-brass powder to fabricate bulk samples. The powder mixtures were subjected to HPT to obtain green compacts [30]. A mini chamber, described by Wurmshuber *et al.* [18], was used to prevent oxidation during compaction. This compaction was performed at a nominal pressure of 12 GPa and a rotational speed of 1.28 rpm for a quarter of a rotation. The compaction anvils have a cavity with 8 mm diameter and 0.3 mm depth. For all further HPT processing, the cavity had a width of 8 mm diameter and 0.15 mm depth. Subsequent HPT steps were performed with a rotational speed of 1.28 rpm at a nominal pressure of 12 GPa. To homogenize the microstructure, the green compacts were subsequently subjected to HPT deformation at 200°C for 30 turns followed by 50 turns at RT. A similar two–stepped process was applied by Wurmshuber *et al.* [7] to tungsten-copper compositions with a copper content of 25 wt.% and 50 wt.%, revealing the necessity of the multi-step processing for a homogenous microstructure evolution. Thereby, one turn corresponds to an equivalent strain of 72 at a radius of 3 mm [38]. Certain specimens were further deformed at 400°C for 50 turns to tailor the grain-size. Additionally, one specimen of the tungsten-α-brass composition was deformed at 550°C for 50 turns after the RT processing step to obtain an even larger grain-size.

2.2. Microstructure characterization

The sample disks were cut into two halves with a wire saw, see Fig. 1. One-half was embedded and mechanically polished to examine the microstructural saturation and homogeneity along the radius. On this specimen, the micro hardness along the radius was measured (HV1, Zwick Roell Durascan 20). The indents were placed on the center line of the disk thickness with a spacing of 0.25 mm between the indents along the radius, see Fig. 1a). Additionally, the microstructure was analyzed by scanning electron microscopy (SEM; Zeiss LEO type 1525, Oberkochen, Germany) along the radius with a step size of 0.5 mm, to obtain a qualitative insight into the microstructural homogeneity and −saturation, depicted in Fig. 1a).

The second halves of the HPT disks were used to perform nanoindentation, analyze the grain-size and characterize the fracture process. Therefore, the disk halves were cut into quarters. One quarter piece was manually ground and polished to a wedge-like shape to reduce the subsequent preparation time for lamella and cantilever cutting, illustrated in Fig. 1a). The final wedge-tip thickness (AD) was between 30 μm and 50 μm. Scanning transmission electron microscopy (STEM; JEOL JEM-2200FS microscope, JEOL Ltd.) was used to analyze the grain-size. Therefore, thin lamellas were manufactured at a disk radius of about 3 mm by focused ion beam milling (FIB; Zeiss Auriga Laser platform), see Fig. 1a). The lamellas were thinned to approximately 100 nm at a 30 kV acceleration voltage and by subsequently reducing the FIB current from 2 nA for coarse milling to 50 pA in the final polishing step.

2.3. Mechanical characterization

2.3.1. Nanoindentation

On the second quarter, nanoindentations (FT-NMT04, FemtoTools AG) were performed with a Berkovich tip to determine the composites Young's moduli. As mentioned above the hardness was only used to assess microstructural saturation, thus the hardness obtained from nanoindentation was neglected. For that, the sample disk quarter was ground and polished on the back and front sides to obtain smooth and parallel surfaces. The final polishing step suspension had a particle size of 0.05 μm. Before measuring, the stiffness of the indentation system was calibrated on fused silica. All indents on the sample were placed at radii above 2 mm, as illustrated by the cyan triangles on the left quarter in Fig. 1a).

2.3.2. Cantilever preparation

The cantilevers were fabricated on the quarter used for the STEM analysis and pre-cut at a radius of approximately 3 mm by femtosecond laser ablation [39] to a cantilever height of about 20 μm, as illustrated in Fig. 1a). The final shaping step of the cantilevers was performed by FIB milling. The current was subsequently reduced from 20 nA for coarse machining to 2 nA in the polishing step. The final cantilevers had a cross-section (W x B) of 10x10 μm^2 with a cantilever length (L) of about 40 μm and an initial notch depth (a) of 0.44 x W. The notch was fabricated by line milling from the top view with a current of 500 pA. Fig. 1b) illustrates schematically the final cantilever geometry with all essential geometric parameters, while Fig. 1c) depicts a final cantilever before *in situ* testing.

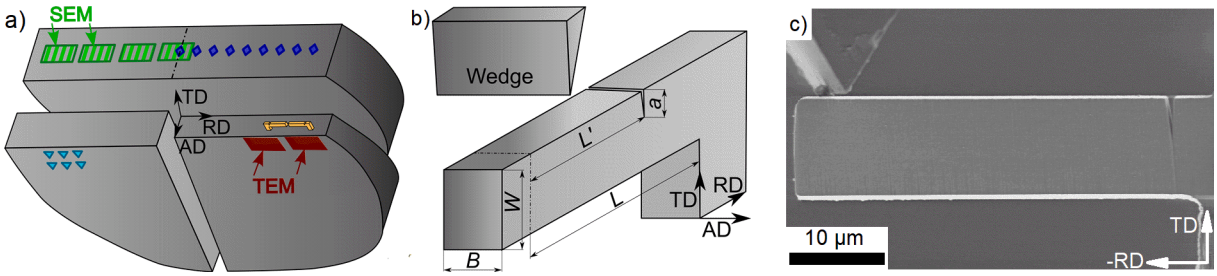

Fig. 1. Sample investigation and preparation steps. a) Disk halves produced by high-pressure torsion illustrating schematically the measurement positions, Vickers hardness measurement (blue diamonds), backscatter electron imaging (green patterned squares), nanoindentation measurements (cyan triangles), micro-cantilever bending beams position (orange) and the scanning transmission electron microscopy lamella position (red rectangles). b) Schematic drawing of a cantilever with all essential geometry parameters. c) *In situ* cantilever before testing. (For interpretation of the references to colour in this figure legend, the reader is referred to the web version of this article.)

2.3.3. Test setup

To test the cantilevers in a displacement–controlled fashion two micro/nano indenters were used; an ASMEC indenter (UNAT SEM 1, ASMEC GmbH) mounted in an SEM (DSM 982, Carl Zeiss AG) and a FemtoTools (FT-NMT04, FemtoTools AG) situated in an SEM (SEM 1525, Carl Zeiss AG). The two different measurement systems were selected to compare the results from different loading conditions, namely partial unloading versus continuous stiffness measurement. Both indenters employed a loading rate of 50 nm/s. The ASMEC indenter had a noise level of 50 µN in the vacuum. To assess the crack length for the elastic–plastic fracture mechanical evaluation, the cantilevers were loaded to a maximum displacement of 16 µm with 15 sequential unloading steps, evenly distributed along the load signal [40]. Each unloading step consisted of a displacement drop of 10% capped at 2 µm. Before and after each unloading, a hold segment of 10 s was employed. The FemtoTools indenter had a noise level of 100 nN in the vacuum and allows superimposing the loading signal with a sinusoidal signal for quasi-continuous stiffness measurement, referred to as dynamic measurement in this work. The imposed signal had an amplitude of 2 nm and a frequency of 200 Hz. Nevertheless, the cantilevers tested by the FemtoTools were elastically pre-loaded up to 400 nm to determine the initial stiffness. After pre-loading, the cantilevers were unloaded and then loaded up to a maximum displacement of 5 µm, upon which all cantilevers exhibited unstable fracture at displacements of about 1 µm. The recording frequency of the FemtoTools indenter was set to 500 Hz. Further, in both setups, an SEM was used to record *in situ* images at a rate of one frame per second using the in-lens secondary electron detector.

2.3.4. Fracture mechanical evaluation

The load–displacement data of all cantilevers exhibited a perceivable non-linearity before fracture, depicted by the representative load–displacement curves in Fig. 2. The inset of Fig. 2 gives a detailed view of the non-linearity before failure. Hence, elastic–plastic fracture mechanics (EPFM) was used to evaluate the fracture experiments. The calculation followed the detailed description given in the literature by Wurster *et al.* [40] to determine the *J*-integral. EPFM necessitates knowledge of the current crack length, which was obtained by associating the stiffness variations to cross-sectional changes, in particular the crack extension [41]. In the case of quasi-static loading, the cantilever stiffness was determined by linearly fitting the unloading segments of the load–displacement curves [40]. For the dynamic measurements, the stiffness was obtained directly during the experiment. Further, to convert the stiffness changes to a crack extension, the initial crack length in combination with the initial cantilever stiffness are required [41]. Therefore, the former was determined postmortem from the fracture surfaces, by measuring the initial crack length at least five times at equidistant locations. The initial stiffness for the quasi-static loading was obtained from the first unloading. In the case of failure before unloading, the loading stiffness was used instead. The initial stiffness for the dynamic measurements was determined by a single elastic pre-loading.

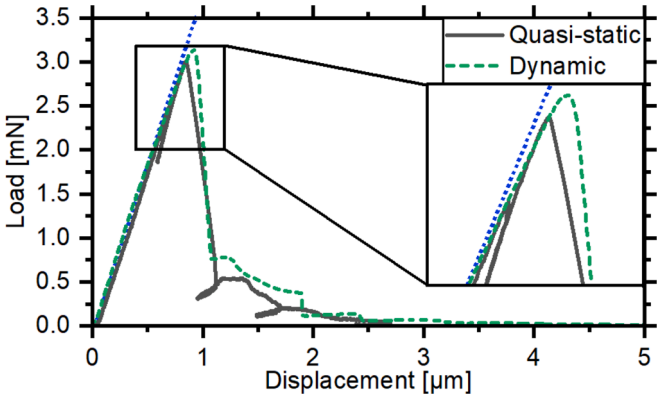

Fig. 2. Representative load–displacement curves recorded from quasi-static or dynamic loading. All samples failed unstable and revealed a non-linearity before failure. The dotted blue line should guide the reader's eyes. (For interpretation of the references to colour in this figure legend, the reader is referred to the web version of this article.)

To determine J_q, the *J*-integral was calculated at the failure point and therefore at the maximum load. For quasi-static loading, which usually allows only evaluation at each distinct unloading, the energy dissipated between the last recorded unloading and fracture were included in the calculation, considering the last measured stiffness.

The determined J_q values were converted into fracture toughness values (K_q), to facilitate a comparison between literature and data from linear-elastic fracture mechanics. The conversion is performed by the equation [42],

$$K_q = \sqrt{\frac{J_q E}{1-\nu^2}} \tag{1}$$

with the Young's modulus E as determined from nanoindentation data and the Poisson ratio $\nu = 0.32$ [43].

3. Result

3.1. Material characterization

All specimens exhibited a constant micro hardness value above a radius of 1.5 mm, indicating a saturated grain-size. The mean hardness values for the tungsten-copper composition above this radius were 8.1 ± 0.1 GPa and 7.9 ± 0.1 GPa for the RT and 400 °C sample, respectively. For the tungsten-α-brass composites, the hardness measurement revealed a mean value of 8.6 ± 0.6 GPa, 9.0 ± 0.3 GPa and 7.6 ± 0.2 GPa for the RT, 400°C and 550°C specimen, respectively. The hardness values are depicted in Fig. 3a). Transparent data points

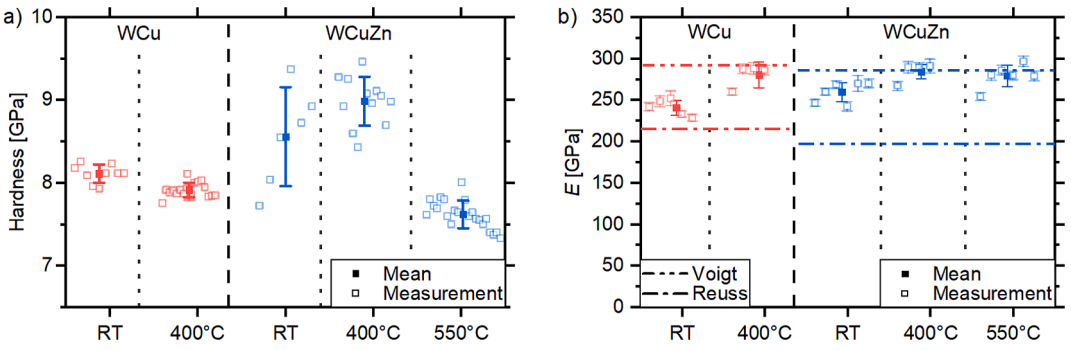

Fig. 3. a) Micro Vickers hardness measurements. b) Young's modulus determined by nanoindentation for the nanostructured tungsten-copper and tungsten-α-brass composites.

represent individual measurements, while opaque ones illustrate the mean and standard deviation for an individual specimen.

The Young's modulus determined for the individual samples are depicted in Fig. 3b). These measurements revealed a Young's modulus of 241 ± 9 GPa and 280 ± 15 GPa for the tungsten-copper composition deformed at RT and 400 °C, respectively. For the tungsten-α-brass composition a Young's modulus of 260 ± 11 GPa, 284 ± 9 GPa and 280 ± 13 GPa was measured for the RT, 400 °C and 550 °C samples, respectively.

The microstructure was analyzed along the HPT disk radius by SEM imaging. From the SEM images no significant microstructural changes were detected above a radius of 1.5 mm, verifying microstructural saturation and homogeneity at higher radii. Nevertheless, the obtained microstructure consisted of a bi-modal structure with coarse globular tungsten grains embedded into a nanocrystalline matrix consisting of tungsten and either copper or α-brass as a second phase. Representative SEM images are illustrated in Fig. 4 for the different compositions and final deformation temperatures. The bright spots in the micrographs represent coarse tungsten grains. A representative coarse grain is illustrated in the respective insets and the green arrows point to further coarse tungsten grains.

The grain-size of the nanocrystalline matrix was analyzed by STEM as depicted in Fig. 5. Additionally, selected area diffraction was performed to verify the nature of the composites, outlined in the supplementary document. To quantify the mean grain-size, several regions per specimen were evaluated utilizing a watershed algorithm for grain segmentation and to avoid a human bias [44,45]. This allowed to analyze a few thousand grains per sample, resulting in a viable statistic for each sample. The grain-size distributions of the respective nanocrystalline matrixes are depicted in Fig. 6 and the essential statistical values of these distributions are listed in Table 1.

3.2. *Fracture mechanical evaluation*

All tested cantilevers failed unstable, and the respective fracture surfaces were analyzed postmortem to characterize the failure type and relate the microstructure to the fracture surface, as depicted in Fig. 7. With increasing grain-size, increasingly rougher fracture surfaces are also obtained, as evident in Fig. 7. The insets in Fig. 7 illustrate a magnified representative coarse tungsten grain present on the fracture surface. The surface roughness observed from the micrographs is comparable to the grain-size present in the individual microstructures. The nanocrystalline matrix grains are unresolved due to the resolution limit of the micrographs. Nevertheless, the structure observed on the fracture surfaces is closely related to the microstructure of the sample, compare Figs. 4 and 7.

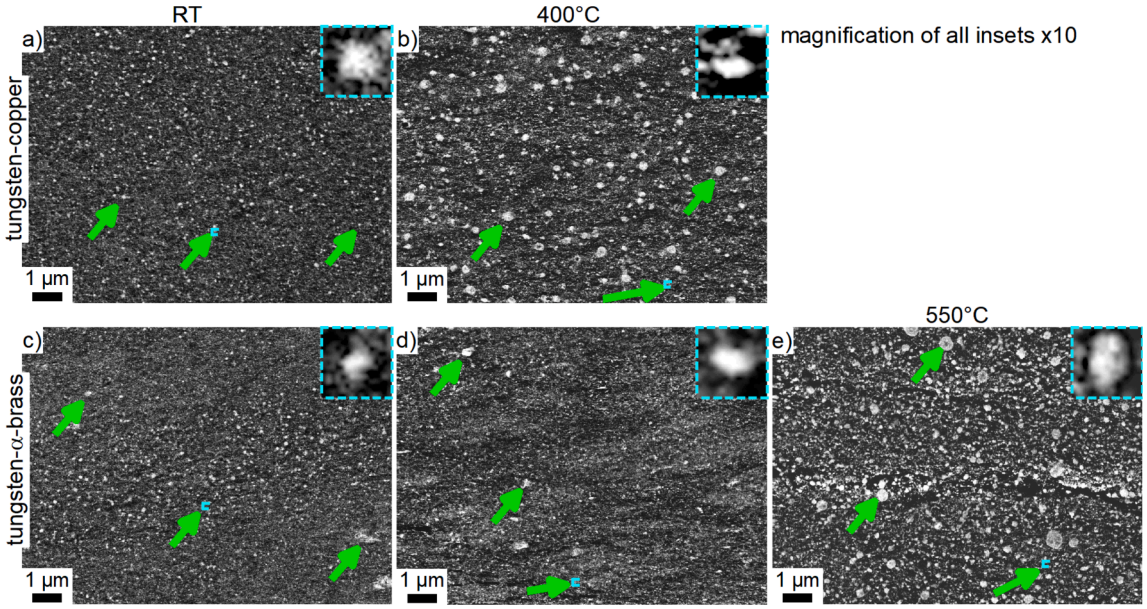

Fig. 4. Representative microstructures of the tungsten-copper (a, b) and tungsten-α-brass (c-e) nanocomposites and varying deformation temperatures recorded by the backscatter electron detector above a disk radius of 1.5 mm. The insets depict representative coarse tungsten grains while the green arrows indicate further coarse tungsten grains. (For interpretation of the references to colour in this figure legend, the reader is referred to the web version of this article.)

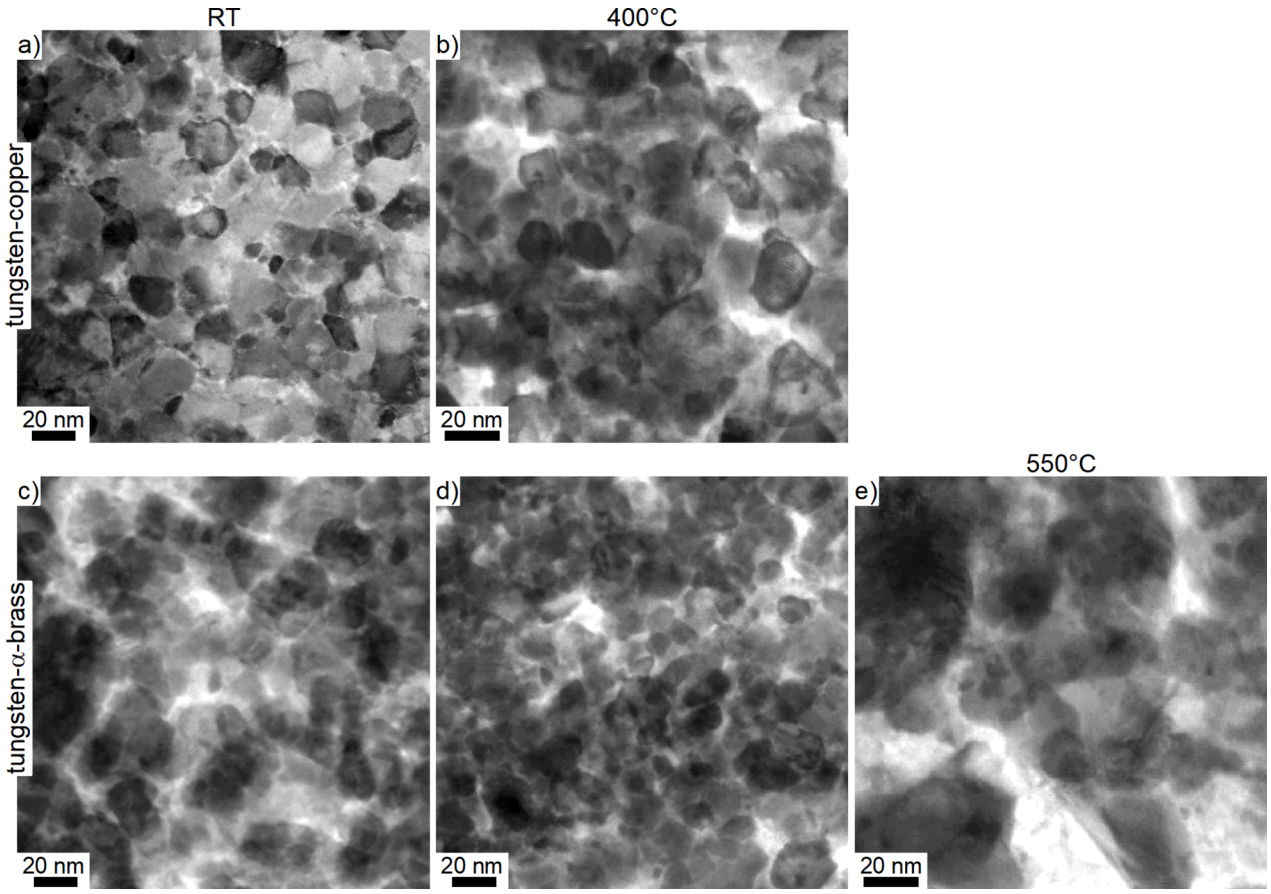

Fig. 5. STEM micrographs to measure the grain-size of the nanocrystalline tungsten-copper (a, b) and tungsten-α-brass (c-e) matrix for varying final deformation temperatures, recorded by scanning transmission electron microscopy.

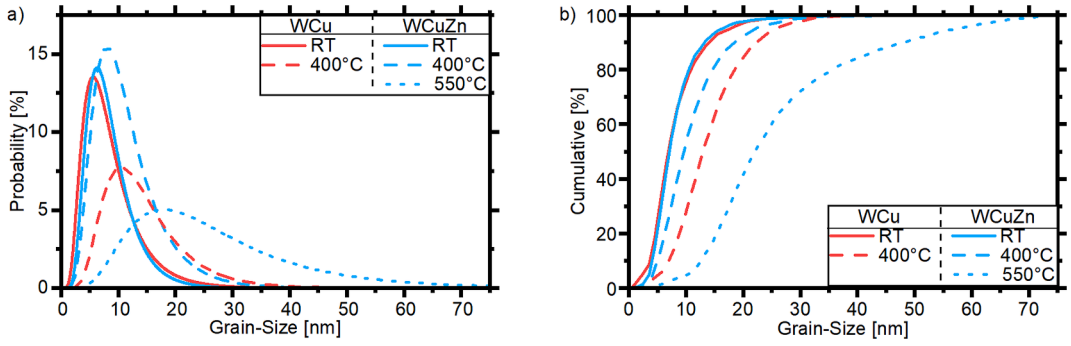

Fig. 6. Grain-size distribution for the tungsten-copper (WCu) and tungsten-α-brass (WCuZn) compositions deformed at different final deformation temperatures, whereby a) depicts the probability density function (pdf) and b) the cumulative density function (cdf). For the colored version, the reader is referred to the online version of this article.

Furthermore, fracture surface recordings were used to determine the initial crack length. For all cantilevers, the initial crack fronts were relatively straight. Nevertheless, the initial crack fronts exhibited some variability, which was estimated by the standard deviation over multiple crack length measurements along the crack front. This resulted in a standard deviation of the crack length for individual cantilevers of 64 nm, 122 nm and 380 nm for the minimum, median and maximum deviation of the crack length, respectively. This in turn results in a relative variation of 1.4%, 2.8% and 7.3% for the minimal, median and maximal variability, respectively.

The mechanical data collected during the fracture experiments was used to calculate the fracture toughness according to EPFM. Fig. 8 depicts the determined J_q values, whereby the transparency of the data points follows the same scheme as before. The measurement error of individual cantilevers was approximated by error propagation, considering the errors from material properties and geometrical measurements. Thereby, the initial crack length measurement error, estimated by the standard deviation from the postmortem initial crack length measurements, impacted the measurement error the most. For tungsten-copper, a mean J_q of $40 \pm 4 \frac{J}{m^2}$ and $36 \pm 2 \frac{J}{m^2}$ was determined for the RT and 400°C samples, respectively. To compare the quasi-static and dynamic setup, two sets of cantilevers were fabricated for the tungsten-α-brass composition deformed at RT. For both loading conditions, the cantilever exhibited a similar load–displacement response and the failure occurred at a displacement of about 1 μm, see the representative

Table 1
Statistics of the grain-size distributions measured for the different sample compositions and final deformation temperatures (T). The given statistical values are: the mean with standard deviation ($\overline{d}$), the median (d_{50}), the 15th-(d_{15}) and 85th percentile (d_{85}). The last column represents the evaluated grain count.

T [°C]	$\overline{d}$ [nm]	d_{50} [nm]	d_{15} [nm]	d_{85} [nm]	Grains [-]
tungsten-copper					
RT	9 ± 6	7	5	13	1693
400 °C	14 ± 6	13	9	21	1892
tungsten-α-brass					
RT	9 ± 5	8	5	12	2897
400 °C	11 ± 6	10	6	17	1515
550 °C	28 ± 16	23	15	43	2302

loading curves in Fig. 2. Though, the calculated J_q evidenced significant difference for quasi-static and dynamic loading, which were 42 ± 4 $\frac{J}{m^2}$ and 29 ± 2 $\frac{J}{m^2}$, respectively. For the tungsten-α-brass samples deformed at elevated temperatures of 400°C and 550°C, a mean J-integral value of 28 ± 4 $\frac{J}{m^2}$ and 37 ± 1 $\frac{J}{m^2}$ was determined. The estimated errors directly correlate to the single measurement scatter. This scatter is increased for the RT sample of both compositions and relates to the more significant variation of $\frac{a_0}{W}$ among the cantilevers. Further, the 400°C tungsten-α-brass sample exhibited an increased scatter as only two cantilevers were tested successfully. This was caused by the loss of cantilevers during sample transfer or invalid tests when the indenter hit some material in the background during loading.

4. Discussion

The next section outlines the possible reasons for the discrepancy between quasi-static and dynamic loading, followed by the discussion of deformation temperature impact on the microstructure. Thereafter, the two composites are compared with each other and finally set into context with literature values.

4.1. Dynamic vs. quasi-static loading

Comparison between the quasi-static and dynamic measurement setup reveals an increased J_q value of about 12 $\frac{J}{m^2}$ for the quasi-statically tested cantilevers, see Fig. 8. This results from the sequential unloading steps, as they share similarities with low cycle fatigue testing. During loading, the material in front of the crack deforms plastically. Throughout the partial unloading, stresses are relieved and partially inverted. This inversion leads to partial recovery of the plastic zone, but also a buildup of compressive stresses and results in the formation of a cyclic plastic zone [46]. Similar findings were reported by Ast *et al.* [47]. They investigated the quasi-static loading and observed a dislocation density reduction during unloading, pointing to plastic recovery. This benefits the J_q values, as this allows to trigger slight hardening effects and enables further energy dissipation during the subsequent loading cycles [48]. Cantilevers that were loaded quasi-statically and failed

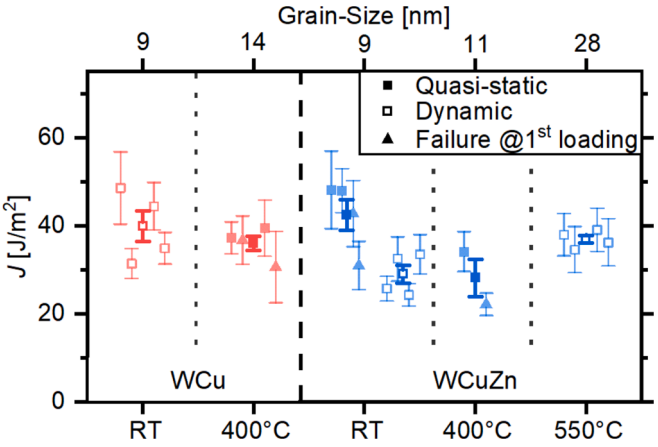

Fig. 8. Fracture characteristics in terms of J-integral determined for the material composition tungsten-copper (WCu) and tungsten-α-brass (WCuZn) by testing single-edge notched bending cantilevers. For the colored version, the reader is referred to the online version of this article.

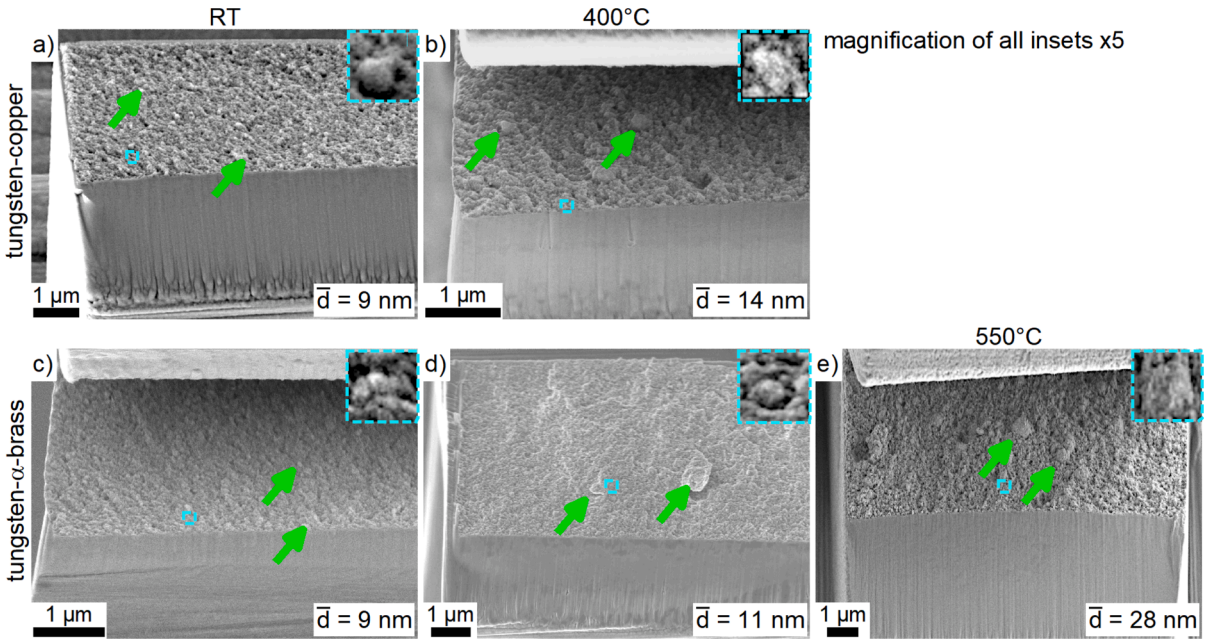

Fig. 7. Postmortem analysis of the fracture surfaces for the tungsten-copper a), b) and the tungsten-α-brass c)-e) composition for the different grain-sizes. A representative coarse tungsten grain is illustrated in the insets, while the green arrows point to further representative coarse tungsten-grains. (For interpretation of the references to colour in this figure legend, the reader is referred to the web version of this article.)

before the first unloading back this assumptions, as these cantilevers exhibited lower J_q values and suggesting that no cyclic plastic zone has evolve, visible in Fig. 8 by the RT tungsten-α-brass composition. Snartland *et al.* [49] reported a similar systematic offset for the fracture toughness determined by quasi-static compared to dynamic loading for single crystal α-iron. This indicates an inherent material and microstructure independent increase for the quasi-static loading condition.

4.2. Grain-size effects

In the case of tungsten-copper the hardness reduced from 8.2 GPa to 7.9 GPa with increasing grain-size from 9 nm to 14 nm, following the common Hall-Petch behavior. For the tungsten-α-brass composite, a raised hardness from 8.6 GPa to 9 GPa was found for a slightly increasing grain-size form 9 nm to 11 nm. Further, grain-size increase reduced the hardness to 7.6 GPa. The measured hardness values are in agreement with literature data, which states 8 GPa for a nanocrystalline tungsten-copper composite with 33 wt.% copper produced by HPT [45]. Comparing the two compositions reveals a hardness increase for the tungsten-α-brass composite of about 12% for a grain-size of 9 nm. This increase can mainly be attributed to the strengthening of the copper phase, resulting in enhanced mechanical properties even at elevated temperatures [50]. Literature reports a hardness increase for alloying copper with zinc to α-brass of about 30% for a composition with micron sized grains [51]. Accounting for the volume ratio of about 48 vol.% of copper and α-brass phase the increase is in agreement with literature.

Recorded SEM micrographs evidenced a direct correlation between final deformation temperature and obtained grain-size, visible by the enlarging of coarse tungsten grains in Fig. 4. Qualitative analysis of the micrographs indicates an increased deformation temperature dependency for the tungsten-copper composition. This is identifiable by the pronounced enlargement of the coarse tungsten grains between RT and 400°C for about 35% compared to about 6% for the tungsten-copper and tungsten-α-brass composite respectively, see Fig. 4. From the STEM recordings a similar trend as by SEM is observable, illustrated in Fig. 5. The quantitative grain-size analysis verified this trend and revealed a direct correlation between grain-size and final deformation temperature. Increasing the deformation temperature induced a higher saturation grain-size [52], as depicted by the grain-size distribution curves in Fig. 6. For the tungsten-copper composition the analysis revealed an relative mean grain-size increase of 50% by raising the deformation temperature from RT to 400°C, see Table 1. Besides the increased mean, the grain-size distribution broadens for the 400°C tungsten-copper sample, resulting in a significant amount of grains above 20 nm, shown by the black dashed distribution in Fig. 6. In the case of tungsten-α-brass the mean grain-size increased only by 22% between RT and 400°C, see Table 1. This modest increase exhibited by the tungsten-α-brass composition occurs due to the harder secondary phase, which supports a pronounced grain refinement. Furthermore, residual elements contribute to a more severe grain refinement during HPT, leading to a lower saturation grain-size at elevated temperatures [53]. Either way, raising the deformation temperature for tungsten-α-brass to 550°C resulted in a grain-size increase of about 300% compared to the RT sample, tabulated in Table 1. This may occur as the brittle to ductile transition temperature of tungsten is about 200°C to 400°C, resulting in a less severe refinement of the grains by tungsten above this temperature [54]. Moreover, the distribution broadened significantly, resulting in a few grains above 50 nm, see the dotted blue distribution curve in Fig. 6. Comparing the two compositions indicates an almost identical microstructure and grain-size for the samples deformed at RT. The grain-sizes obtained are in accordance with literature, which reports for HPT refined tungsten-copper samples fabricated from bulk a mean grain-size of 9 nm and 14 nm for a composition with 20 wt.% and 33 wt.% copper, respectively [55,56]. Literature states for a bulk tungsten-copper composite with 20 wt% copper deformed by HTP at 400°C a grain-size of 28 nm. In this work 14 nm was found. This difference might stem from the use of powder precursor, which are prone to degradation, *e.g.* by oxides. These degradations may reinforce the processed material and affect the refinement process [57]. Similarly, the grain-size deviation for the investigated tungsten-α-brass composites may have a similar origin, as copper and zinc were alloyed by ball-milling.

Relating the hardness to the microstructure for the tungsten-copper composition, the hardness decrease confirms the common Hall-Petch behavior [19–21,58]. In the case of the tungsten-α-brass composition, correlating the grain-size with the hardness values evidences the transition from normal to inverse Hall-Petch characteristics. The latter occurs between samples with a grain-size of 9 nm and 11 nm. Further, by increasing the grain-size up to 28 nm the hardness decreases and indicates common Hall-Petch behavior. The grain-size for this transition from normal to inverse Hall-Petch is debated in literature, several studies investigated this transition for copper and platinum and reported a transition for grain-sizes in the range of 10 nm to 20 nm [22–25,58].

4.3. Specimen density

The nanoindentation measurements evidence a slight correlation between final deformation temperature and Young's modulus, see Fig. 3b). The lower and upper bound of Young's modulus can be approximated by the Reuss and Voigt model [59,60]. To approximate the bounds a Young's modulus of 410 GPa [18,61], 130 GPa [62] and 115 GPa [63] are assumed for tungsten, copper and α-brass. This gives estimated bounds of 215 GPa and 292 GPa for the tungsten-copper composition, and in the case of tungsten-α-brass 197 GPa and 286 GPa, respectively. All measured Young's moduli are within the boundaries given by the Reuss and Voigt model, see the Fig. 3b).

Moreover, literature states that Young's modulus differences of the same material can be correlated to the material's porosity [64,65] by

$$E = E_0(1 - 1.9p + 0.9p^2), \tag{2}$$

with p the porosity, E the measured Young's modulus and E_0 the Young's modulus of a fully dense sample. The material density is then given by $1 - p$. To qualitatively estimate the density of the sample, the upper bound value was used for E_0, which is 292 GPa and 286 GPa for the tungsten-copper and tungsten-α-brass composition. This gives for the former a density of approximately 91.4% and 98.4% for the RT and 400°C samples, respectively. In the case of the tungsten-α-brass composition fabricated at RT, 400°C and 550°C a density of 92.4%, 99.6% and 99.1% was estimated. These approximated densities indicate a qualitative trend across the compositions, where increased temperature enhance the sample density. This is likely a result of the interaction between mechanical and thermal assisted compaction phenomena, similar to sintering. Moreover, adding zinc increases the achieved density slightly, which can be related to the reduced sintering temperature [66]. As the density of the tungsten-α-brass sample is even higher, this would support such an argument. In comparison, literature reports a material density of 90–95%, 98.6%, 98–99% and 99.8% for liquid sintering, activated liquid phase sintering, hot-shock consolidation and liquid sintering in combination with hot-hydrostatic extrusion, respectively [5,8]. Despite the qualitative nature of the estimated densities, the individual sample densities are comparable to conventional sintering methods.

Anyways, an approximate porosity of about 10% should be observable in the SEM micrographs. Though, in the recorded micrographs no pores were observed. In addition, a porosity of 10% would significantly reduce the materials hardness. Comparing the hardness values reveals an increasing hardness with decreasing grain-size for the tungsten-copper composition. For the tungsten-α-brass sample the hardness decreased with decreasing the grain-size from 11 nm to 9 nm. Thus, porosity as the main cause for Young's modulus variations can be ruled out, as only small hardness changes are observed for the investigated material compositions. A further possibility for a decreased Young's

modulus is a change in contact area, which might occur due to the transition of deformation mechanisms. Trelewicz *et al.* [67] reported for tungsten-nickel composites with a grain-size ranging between 20 nm and 3 nm a change from a homogenous, smooth to an inhomogeneous, stepped pile-up during nanoindentation. They argued that this originates in the transition from a conventional homogenous plasticity to unstable plastic flow from a grain-size of 20 nm to 3 nm. No such changes were observed from the nanoindentation imprints performed in this work. Thus, a similar deformation mechanism among all samples and a negligible impact of possible contact area variation are expected. Another possibility is the significantly raised grain boundary volume, which exhibits a reduced stiffness and affects the Young's modulus measurement [25,68,69]. To roughly estimate the grain boundary volume, the ratio between the grain surface and volume can be used. Estimating this for the tungsten-copper composition with a grain-size of 9 nm and 14 nm this yields an increase of 57%. In the case of tungsten-α-brass sample an increase of 22% can be expected. Hence, the decreased Young's modulus for the RT samples can be attributed to the increased grain boundary volume fraction.

4.4. Characterizing fracture

From the fracture surfaces the two investigated material compositions are hardly differentiable, as both exhibit a similar surface structure, illustrated in Fig. 7. Qualitatively, the structural feature sizes increase with increasing deformation temperature for both compositions. Relating the grain-size to the respective structural size on the fracture surfaces indicates an inter-crystalline failure for all cantilevers. An exact characterization of the fracture behavior is challenging, as the local crack path is hardly identifiable due to the relatively small grain-size. However, in the case of the tungsten-α-brass with a grain-size of 28 nm, deviation of the crack path along larger surface features is more clearly visible, see Fig. 7e). This suggests a generally high amount of inter-crystalline fracture, as it is expected for these nanometer-scaled grain-sizes [70–72]. Additionally, TEM investigations were carried out near the fracture surface to analyze possible grain coarsening due to the applied deformation. From these investigations, no significant grain coarsening was observed.

The fracture mechanical evaluation of the tungsten-copper compositions indicates an inverse relation between grain-size and determined J_q, as J_q is slightly reduced for a grain-size of 14 nm (400°C), visible in Fig. 8. Additionally, considering the systematic offset between the quasi-static and dynamic measurement approach, this difference would increase as described above. Hence, increasing the grain-size from 9 nm to 14 nm has drawbacks for the J_q. An increasing grain-size enhances the tendency for dislocation-nucleation based deformation [26,73,74]. Literature reports the transition from grain-boundary mediated to dislocation-nucleation based mechanism at a grain-size of about 30 nm for bcc materials such as tungsten [27]. However, the majority of the deformation will be localized in the softer copper phase, which has an fcc crystal structure. From the literature, a transition grain-size of about 10 nm between dislocation-nucleation based and grain boundary-mediated processes is known [26]. Despite the possibly increased tendency for dislocation-nucleation due to the coarsened microstructure from 9 nm to 14 nm, the dominated deformation mechanism is grain boundary mediated, as analysis of the fracture surfaces reveal an inter-crystalline failure. Thus, the decrease of J_q can be attributed to the decreasing grain boundary cohesive strength with increasing grain-size, countering the possible positive effects stemming from a longer crack path and the additional deformation mechanism [75,76].

For the tungsten-α-brass composition, the grain-size increase is less pronounced from 9 nm to 11 nm by raising the deformation temperature from RT to 400°C, respectively. Though, the J_q decreased for the latter. Quasi-static testing of both grain-sizes makes the trend clearly visible, illustrated in Fig. 8. This trend is similar to the tungsten-copper composition and points to an analogous behavior of a reduced grain boundary cohesion strength. In contrast, the larger grain-size of 28 nm (550°C) reverts the trend and exhibits an average increase of 37% in J_q compared to the RT values. On one hand the larger grains increase the crack path length, allowing to dissipate more energy during crack growth. On the other hand, the grain-size of 28 nm significantly enhances the dislocation-nucleation tendency, providing the possibility to dissipate additional energy. Moreover, a grain-size of 28 nm is closer to the ideal grain-size for an extensive twinning tendency. Literature reports an ideal grain-size of 40 nm to enable twinning as an additional deformation mechanism in pure copper and α-brass with 10 wt.% zinc [36,37]. Below this grain-size, twinning is increasingly challenging due to de-twinning caused by the interaction between partial dislocations and twin boundaries [77]. Despite the significant grain-size increase achieved by raising the deformation temperature, all samples exhibit a grain-size below the ideal grain-size for twinning. However, the considerable increase in grain-size by HPT deformation at 550°C supports an argument for some additional contribution of an enhanced dislocation-nucleation and twinning tendency during fracture, thereby increasing J_q.

Comparison of both compositions reveals that the obtained J_q values are on the same order of magnitude. Nevertheless, the J_q values of tungsten-α-brass are slightly below the tungsten-copper results, despite the enhanced density, visible in Fig. 8. A possible explanation for this is the damage introduced by focused ion beam milling of the notch. From literature, it is known that zinc and α-brass are prune to liquid metal embrittlement from gallium [78]. Hence, to rule out possible embrittlement of the tungsten-α-brass composition during the cantilever fabrication, the penetration depth of gallium was simulated by SRIM [79]. For the simulation the Kinchin-Pease algorithm was used [80]. The acceleration voltage of the gallium ions was set to 30 keV with an incidence beam angle of 0°. This revealed a penetration depth of about 50 nm, 30 nm and 30 nm of gallium in pure zinc, α-brass and the tungsten-α-brass composition, respectively. Due to the small penetration depth, a major impact on the J_q values from liquid metal embrittlement can be neglected. Hence, the reduced J_q might result from minor additional incorporation of impurities during the required ball milling step to alloy copper and zinc. During this step, traces of residual elements from vial and grinding balls are dissolved in the powder [81]. Nevertheless, in x-ray diffraction measurements of the α-brass powder, such elements were undetected [35]. Still, due to the resolution limit of x-ray diffraction these elements have to be considered and may impact J-integral values.

4.5. Comparing toughness to similar material systems

The determined J_q values were converted into conditional linear-elastic fracture toughness K_q to facilitate correlation with literature data. This results in a K_q of 3.3 ± 0.1 MPa$\sqrt{\text{m}}$ and 3.3 ± 0.2 MPa$\sqrt{\text{m}}$ for the tungsten-copper composites fabricated at RT and 400 °C, respectively. For the tungsten-α-brass, the conversion yields 3.2 ± 0.1 MPa$\sqrt{\text{m}}$, 3.0 ± 0.2 MPa$\sqrt{\text{m}}$ and 3.4 ± 0.1 MPa$\sqrt{\text{m}}$ for the RT, 400°C and 550°C sample, respectively. Schmuck *et al.* [55] reports a K_q value of 7.4 MPa$\sqrt{\text{m}}$ for a nanocrystalline tungsten-copper composite with 20 wt.% copper. They used as base material bulk and performed a single HPT step to refine the grains, leading to a mean grain-size of 28 nm. For a bulk tungsten-copper composite with 50 wt.% copper deformed by HPT to a mean grain-size of 10 nm, literature reports a K_q value of 8.1 MPa$\sqrt{\text{m}}$ [82]. The investigated samples in this work exhibited lower K_q values and were produced from powders, which may impact K_q, as powder particles have a high surface to volume ratio and are therefore prone to degradation, *e.g.* oxidation. Oxygen segregation to grain boundaries is known to reduce the interface adhesion, weaken the grain boundaries and form brittle phases [83]. Although the powders were always handled in an argon atmosphere, slight degradation is

challenging to avoid. In addition to oxidation, ball milling may introduce traces of residual elements from vials and grinding balls. Consequently, samples produced from powders are typically sintered in a reduction atmosphere to eliminate oxides and other potential volatile degradation. As a reducing atmosphere, hydrogen is frequently used for high temperature sintering. In this atmosphere in combination with high temperature zinc tends to evaporate and the zinc content will decrease significantly [84,85]. Another possibility would be sintering at low pressures to remove volatile degradation, but due to the vapor pressure of zinc and copper this is unfeasible At usual sintering temperatures of around 1250°C the vapor pressure of zinc and copper is about > 10 bar and 0.012 mbar, respectively [86]. Either way, for pure nanocrystalline tungsten produced by magnetron sputtering with a grain-size of 30 nm, literature states a K_q of 2.4 MPa$\sqrt{\text{m}}$ [87,88]. A higher K_q for the compositions investigated in this work was found, indicating the potential to enhance the damage and fracture tolerance of tungsten by adding a copper as ductile phase.

Moreover, to unravel the relation between K_q and the grain-size, various literature sources were collected to identify possible trends. These points are illustrated in Fig. 9 including the K_q values reported in this present study. In the case of pure polycrystalline tungsten all data points fabricated from sintered bulk samples are above the nanocrystalline regime. Their K_q declines with decreasing the grain-size from the coarse to the ultra-fine grained regime. This occurs as tungsten is prone to inter-crystalline failure. Thus, the grain boundaries significantly impact the fracture process. For coarse grained materials the grain boundaries are less intrinsically stressed, allowing to accommodate more plasticity [89]. Though, on the lower end of the ultra-fine grained regime Wurmshuber *et al.* [90] reported a strong increase of the K_q to 22 MPa$\sqrt{\text{m}}$ for pure tungsten produced from elemental powders. The powder processing route allows to dope the composition to further enhance the mechanical properties of tungsten. They sintered the green compacts and subsequently refined the microstructure by HPT. However, sputtered tungsten with a nanocrystalline microstructure exhibits a low K_q of about 2.4 MPa$\sqrt{\text{m}}$ [87,88]. Beside the grain-size influence this reduced K_q can be partially attributed to the absence of sintering in the fabrication process. This assumption is backed by the lower K_q values obtained for coarse grained tungsten produced by chemical vapor deposition [91]. Sintering activates diffusion and the grain boundaries get better interconnected, benefiting K_q. In the case of tungsten-copper composites literature lacks data in the ultra-fine grained regime, thus a trend is hardly identifiable over the different magnitudes of grain-sizes. Nevertheless, the coarse grain-sizes exhibit a higher K_q compared to nanocrystalline microstructures. This might stem from the significantly increased amount of grain boundaries in the nanocrystalline regime, similarly as for pure tungsten between the coarse and ultra-fine grained regime. Though in the nanocrystalline regime a slightly inverse relation between fracture toughness and grain-size is observable, which might indicate a transition from dislocation to grain boundary based deformation mechanism. Moreover, tungsten-composites produced from powders without sintering revealed a decreased K_q compared to sintered samples, which points to a similar origin as stated above. Nevertheless, nanocrystalline tungsten-copper composites produced from elemental powders exhibit an enhanced K_q compared to pure sputtered tungsten in the nanocrystalline regime, indicating the potential to raise the damage and fracture tolerance by such nanocomposite design.

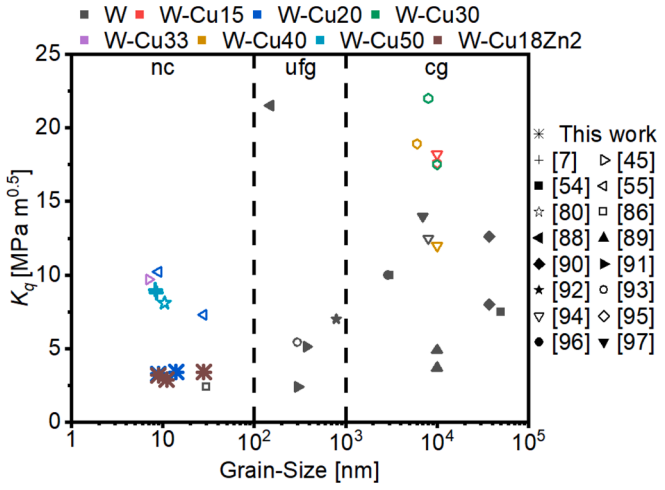

Fig. 9. Comparison of the fracture toughness for various grain-sizes of polycrystalline tungsten-based composites in coarse grained (cg), ultra-fine grained (ufg) and nanocrystalline (nc) regime [7,45,54,55,82,88,90–99].

5. Conclusion

In this work, tungsten-copper and tungsten-α-brass nanocomposites were produced starting from elemental powders. The powders were compacted and subjected to multiple high-pressure torsion steps to refine the grains to the nanocrystalline regime. These investigations revealed a correlation between the deformation temperature and the obtained grain-size. Raising the temperature from RT to 400°C increased the mean grain-size for tungsten-copper from 9 nm to 14 nm. In comparison, the grain-size achieved for the tungsten-α-brass composition was 9 nm, 11 nm and 28 nm for the RT, 400°C and 550°C specimens, respectively. Young's modulus measurements revealed an increase from RT to the elevated temperatures, which is likely a result of the reduced grain boundary volume. Notched cantilever bending beams were fabricated from the deformed sample material to examine the fracture behavior. Despite the grain-size increase for both compositions, the J-integral values decreased slightly from RT to 400°C, which might stem from a declining grain boundary cohesion strength with increasing grain-size. Enlarging the grain-size leads to an increase in conditional J-integral values, which indicates an increased dislocation-accumulation tendency and the activation of twinning in the tungsten-α-brass composition. Based on the observation in this work, the evaluated fracture performance in terms of J-integral values are on the same order of magnitude and comparable to other nanocrystalline tungsten based materials. However, the addition of zinc improved the other mechanical properties, such as Young's modulus and hardness, which translates into an overall enhanced damage tolerance for such nanocrystalline materials envisioned for use in harsh environments.

6. Availability of data and materials

The data generated during the current study are available from the corresponding author on a reasonable request.

CRediT authorship contribution statement

K. Schmuck: Writing – review & editing, Writing – original draft, Methodology, Data curation, Conceptualization. **M. Burtscher:** Writing – review & editing, Methodology, Data curation. **M. Alfreider:** Writing – review & editing, Methodology. **D. Kiener:** Writing – review & editing, Supervision, Resources, Project administration, Funding acquisition, Conceptualization.

Declaration of competing interest

The authors declare that they have no known competing financial interests or personal relationships that could have appeared to influence the work reported in this paper.

Acknowledgments

This work was supported by European Research Council [Grant number: 771146 (TOUGHIT)]. The authors thank Simon Fellner to help with the TEM lift outs and Nadine Buchebner for performing the nano-indentation measurements. Also, this research was funded by the Austrian Science Fund (FWF) [P 34840-N]. For the purpose of open access, the author has applied a CC BY public copyright license to any Author Accepted Manuscript version arising from this submission.

Appendix A. Supplementary data

Supplementary data to this article can be found online at https://doi.org/10.1016/j.matdes.2024.113433.

Data availability

Data will be made available on request.

References

[1] L. Dong, W. Chen, L. Hou, N. Deng, C. Zheng, W–Cu system: synthesis, modification, and applications, Powder Metall. Met. Ceram. 56 (3–4) (2017) 171–184, https://doi.org/10.1007/s11106-017-9884-6.
[2] D. Sun, Y. Wang, S. Huang, J. Zhao, G. Liu, J. Li, Plasma facing component with built-in tungsten wires and a W-Cu functionally graded layer: a finite element assessment, Fusion Eng. Des. 120 (2017) 9–14, https://doi.org/10.1016/j.fusengdes.2017.05.006.
[3] W. Chen, L. Dong, H. Zhang, J. Song, N. Deng, J. Wang, Microstructure characterization of W-Cu alloy sheets produced by high temperature and high pressure deformation technique, Mater. Lett. 205 (2017) 198–201, https://doi.org/10.1016/j.matlet.2017.06.090.
[4] E. Tejado, A.V. Müller, J.H. You, J.Y. Pastor, Evolution of mechanical performance with temperature of W/Cu and W/CuCrZr composites for fusion heat sink applications, Mater. Sci. Eng. A 712 (December 2017) (2018) 738–746, https://doi.org/10.1016/j.msea.2017.12.054.
[5] L.L. Dong, M. Ahangarkani, W.G. Chen, Y.S. Zhang, Recent progress in development of tungsten-copper composites: fabrication, modification and applications, Int. J. Refract. Met. Hard Mater. 75 (February) (2018) 30–42, https://doi.org/10.1016/j.ijrmhm.2018.03.014.
[6] C. Hou, et al., W–Cu composites with submicron- and nanostructures: progress and challenges, NPG Asia Mater., 11(1), (2019). doi: 10.1038/s41427-019-0179-x.
[7] M. Wurmshuber, et al., Mechanical performance of doped W-Cu nanocomposites, Mater. Sci. Eng. A 857 (September) (2022) 144102, https://doi.org/10.1016/j.msea.2022.144102.
[8] B. Zhang, K. Yang, Z. Huang, J. Wang, Recent advances in W-Cu composites: a review on the fabrication, application, property, densification, and strengthening mechanism, Adv. Eng. Mater. 2301204 (2023) 1–34, https://doi.org/10.1002/adem.202301204.
[9] W. Guo, J. Liu, Y. Xiao, S. Li, Z. Zhao, J. Cao, Comparison of penetration performance and penetration mechanism of w-cu shaped charge liner against three kinds of target: Pure copper, carbon steel and Ti-6Al-4V alloy, Int. J. Refract. Met. Hard Mater. 60 (2016) 147–153, https://doi.org/10.1016/j.ijrmhm.2016.07.015.
[10] H. Chen, et al., Low thermal expansion metal composite-based heat spreader for high temperature thermal management, Mater. Des. 208 (2021) 109897, https://doi.org/10.1016/j.matdes.2021.109897.
[11] H. Xie, et al., W–Cu/Cu composite electrodes fabricated via laser surface alloying, Mater. Charact. 185 (October 2021) (2022) 111715, https://doi.org/10.1016/j.matchar.2021.111715.
[12] S. Su, Y. Lu, Densified W[sbnd]Cu composite fabricated via laser additive manufacturing, Int. J. Refract. Met. Hard Mater. 87 (September 2019) (2020) 105122, https://doi.org/10.1016/j.ijrmhm.2019.105122.
[13] D.I. Tishkevich, et al., Isostatic Hot Pressed W-Cu Composites with Nanosized Grain Boundaries: Microstructure, Structure and Radiation Shielding Efficiency against Gamma Rays, Nanomaterials 12 (10) (2022) 1–14, https://doi.org/10.3390/nano12101642.
[14] A.V. Muller, et al., Melt infiltrated tungsten–copper composites as advanced heat sink materials for plasma facing components of future nuclear fusion devices, Fusion Eng. Des. 124 (2017) 455–459, https://doi.org/10.1016/j.fusengdes.2017.01.042.
[15] X. Chen, W. Sun, X. Li, X. Wang, H. Yan, K. Li, Experimental and numerical studies on W-Cu functionally graded materials produced by explosive compaction–welding sintering, Fusion Eng. Des. 137 (July) (2018) 349–357, https://doi.org/10.1016/j.fusengdes.2018.10.016.
[16] M. Wurmshuber, et al., Enhancing mechanical properties of ultrafine-grained tungsten for fusion applications, Int. J. Refract. Met. Hard Mater. 111 (October 2022) (2023) 106125, https://doi.org/10.1016/j.ijrmhm.2023.106125.
[17] A. Khalajhedayati, Z. Pan, T.J. Rupert, Manipulating the interfacial structure of nanomaterials to achieve a unique combination of strength and ductility, Nat. Commun. 7 (2016), https://doi.org/10.1038/ncomms10802.
[18] M. Wurmshuber, S. Doppermann, S. Wurster, D. Kiener, Ultrafine-grained Tungsten by High-Pressure Torsion - Bulk precursor versus powder processing route, IOP Conf. Ser. Mater. Sci. Eng. 580 (1) (2019) 012051, https://doi.org/10.1088/1757-899X/580/1/012051.
[19] R.W. Armstrong, 60 years of hall-petch: Past to present nano-scale connections, Mater. Trans. 55 (1) (2014) 2–12, https://doi.org/10.2320/matertrans.MA201302.
[20] E.O. Hall, The deformation and ageing of mild steel: III Discussion of results, Proc. Phys. Soc. Sect. B 64 (9) (1951) 747–753, https://doi.org/10.1088/0370-1301/64/9/303.
[21] N. Petch, The cleavage strength of polycrystals, J. Iron Steel Res. Int. 174 (1953) 25–28.
[22] Z. Zhao, S. To, J. Wang, G. Zhang, Z. Weng, A review of micro / nanostructure effects on the machining of metallic materials, Mater. Des. 224 (2022) 111315, https://doi.org/10.1016/j.matdes.2022.111315.
[23] D.A. Konstantinidis, E.C. Aifantis, On the 'anomalous' hardness of nanocrystalline materials, Acta Metall. 10 (7) (1999) 1111–1118.
[24] J.E. Carsley, J. Ning, W.W. Milligan, S.A. Hackney, E.C. Aifantis, A simple , mixtures-based model for the grain size dependence of strength in nanophase, Nanostruct. Mater., no. 4, 1995.
[25] J. Liu, X. Fan, W. Zheng, D.J. Singh, Y. Shi. Nanocrystalline gold with small size: inverse Hall – Petch between mixed regime and super-soft regime, 6435(May), 2020, https://doi.org/10.1080/14786435.2020.1765039.
[26] S. Cheng, J.A. Spencer, W.W. Milligan, Strength and tension/compression asymmetry in nanostructured and ultrafine-grain metals, Acta Mater. 51 (15) (2003) 4505–4518, https://doi.org/10.1016/S1359-6454(03)00286-6.
[27] G.M. Cheng, W.W. Jian, W.Z. Xu, H. Yuan, P.C. Millett, Y.T. Zhu, Grain size effect on deformation mechanisms of nanocrystalline bcc metals, Mater. Res. Lett. 1 (1) (2013) 26–31, https://doi.org/10.1080/21663831.2012.739580.
[28] L. Wang, Z. Zhang, X. Han, In situ experimental mechanics of nanomaterials at the atomic scale, in: NPG Asia Materials 5, Nature Publishing Group, 2013, pp. e40–11, https://doi.org/10.1038/am.2012.70.
[29] Q. Zhang, S. Liang, B. Hou, L. Zhuo, The effect of submicron-sized initial tungsten powders on microstructure and properties of infiltrated W-25 wt.% Cu alloys, Int. J. Refract. Met. Hard Mater. 59 (2016) 87–92, https://doi.org/10.1016/j.ijrmhm.2016.05.014.
[30] D. Jia, Y.M. Wang, K.T. Ramesh, E. Ma, Y.T. Zhu, R.Z. Valiev, Deformation behavior and plastic instabilities of ultrafine-grained titanium, Appl. Phys. Lett. 79 (5) (2001) 611–613, https://doi.org/10.1063/1.1384000.
[31] Y.T. Zhu, X. Liao, Retaining ductility, Nat. Mater. 3 (6) (2004) 351–352, https://doi.org/10.1038/nmat1141.
[32] Z. Budrovic, H. Van Swygenhoven, P.M. Derlet, S. Van Petegem, B. Schmitt, Plastic deformation with reversible peak broadening in nanocrystalline nickel, Science (80-.) 304 (5668) (2004) 273–276, https://doi.org/10.1126/science.1095071.
[33] Y.H. Zhao, X.Z. Liao, S. Cheng, E. Ma, Y.T. Zhu, Simultaneously increasing the ductility and strength of nanostructured alloys, Adv. Mater. 18 (17) (2006) 2280–2283, https://doi.org/10.1002/adma.200600310.
[34] Y.H. Zhao, X.Z. Liao, Z. Horita, T.G. Langdon, Y.T. Zhu, Determining the optimal stacking fault energy for achieving high ductility in ultrafine-grained Cu-Zn alloys, Mater. Sci. Eng. A 493 (1–2) (2008) 123–129, https://doi.org/10.1016/j.msea.2007.11.074.
[35] G. Holub, Simultaneously increasing strength and ductility of nano-crystalline Cu-Zn-alloys made from powderous raw materials, Montanuniversitaet Leoben (2023), https://doi.org/10.34901/MUL.PUB.2023.13.
[36] Y. T. Zhu, X. Z. Liao, S. G. Srinivasan, and E. J. Lavernia, "Nucleation of deformation twins in nanocrystalline face-centered-cubic metals processed by severe plastic deformation," J. Appl. Phys., vol. 98, no. 3, 2005, doi: 10.1063/1.2006974.
[37] Y.T. Zhu, X.Z. Liao, X.L. Wu, J. Narayan, Grain size effect on deformation twinning and detwinning, J. Mater. Sci. 48 (13) (2013) 4467–4475, https://doi.org/10.1007/s10853-013-7140-0.
[38] R. Pippan, S. Scheriau, A. Hohenwarter, and M. Hafok, "Advantages and limitations of HPT: A review", Mater. Sci. Forum, vol. 584–586 PA, pp. 16–21, 2008, https://doi.org/10.4028/www.scientific.net/msf.584-586.16.
[39] M.J. Pfeifenberger, et al., The use of femtosecond laser ablation as a novel tool for rapid micro-mechanical sample preparation, Mater. Des. 121 (2017) 109–118, https://doi.org/10.1016/j.matdes.2017.02.012.
[40] S. Wurster, C. Motz, R. Pippan, Characterization of the fracture toughness of micro-sized tungsten single crystal notched specimens, Philos. Mag. 92 (14) (2012) 1803–1825, https://doi.org/10.1080/14786435.2012.658449.
[41] M. Alfreider, S. Kolitsch, S. Wurster, D. Kiener, An analytical solution for the correct determination of crack lengths via cantilever stiffness, Mater. Des. 194 (2020) 3–7, https://doi.org/10.1016/j.matdes.2020.108914.
[42] "ASTM Standard 1820," ASTM B. Stand., no. January, pp. 1–54, 2013, https://doi.org/10.1520/E1820-13Copyright.
[43] H. Ledbetter, S.K. Datta, Elastic constants of a Tungsten-particle copper-matrix composite, JSME Int. J. Ser. A Solid Mech. Mater. Eng. 34 (April) (1991) 2017, https://doi.org/10.1299/jsmea1988.34.2.
[44] R. Achanta, A. Shaji, K. Smith, A. Lucchi, P. Fua, and S. Süsstrunk, "Slic Superpixels Compared to State-of-the-Art Superpixels Methods," IEEE Trans. Pattern Anal. Mach. Intell., vol. 34, no. 11, pp. 2274–2281, 2012, [Online]. Available: http://ci.nii.ac.jp/naid/110006251524/.
[45] M. Burtscher, M. Alfreider, C. Kainz, K. Schmuck, D. Kiener, In situ micromechanical analysis of a nano-crystalline W-Cu composite, Mater. Des. 220 (2022) 110848, https://doi.org/10.1016/j.matdes.2022.110848.

[46] S. Ghodrat, A.C. Riemslag, L.A.I. Kestens, Measuring plasticity with orientation contrast microscopy in aluminium 6061–T4, Metals (Basel) 7 (4) (2017) 1–8, https://doi.org/10.3390/met7040108.
[47] J. Ast, B. Merle, K. Durst, M. Göken, Fracture toughness evaluation of NiAl single crystals by microcantilevers - a new continuous J-integral method, J. Mater. Res. 31 (23) (2016) 3786–3794, https://doi.org/10.1557/jmr.2016.393.
[48] B.D. Snartland, A.B. Hagen, C. Thaulow, Fracture mechanical testing of single crystal notched α iron micro cantilevers, Eng. Fract. Mech. 175 (2017) 312–323, https://doi.org/10.1016/j.engfracmech.2017.01.024.
[49] B.D. Snartland, C. Thaulow, Fracture toughness testing at the microscale: The effect of the unloading compliance method, Eng. Fract. Mech. 235 (June) (2020) 107135, https://doi.org/10.1016/j.engfracmech.2020.107135.
[50] P. Feltham, G.J. Copley, Yielding and work-hardening in alpha-brasses, Acta Metall. 8 (8) (1960) 542–550, https://doi.org/10.1016/0001-6160(60)90108-5.
[51] P. Chen, G. Luo, M. Li, Q. Shen, L. Zhang, Effects of Zn additions on the solid-state sintering of W-Cu composites, Mater. Des. 36 (2012) 108–112, https://doi.org/10.1016/j.matdes.2011.10.006.
[52] R. Pippan, S. Scheriau, A. Taylor, M. Hafok, A. Hohenwarter, A. Bachmaier, Saturation of fragmentation during severe plastic deformation, Annu. Rev. Mater. Res. 40 (1) (2010) 319–343, https://doi.org/10.1146/annurev-matsci-070909-104445.
[53] R. Tejedor, K. Edalati, J.A. Benito, Z. Horita, J.M. Cabrera, High-pressure torsion of iron with various purity levels and validation of Hall-Petch strengthening mechanism, Mater. Sci. Eng. A 743 (2019) 597–605, https://doi.org/10.1016/j.msea.2018.11.127.
[54] A. Giannattasio, Z. Yao, E. Tarleton, S.G. Roberts, Brittle-ductile transitions in polycrystalline tungsten, Philos. Mag. 90 (30) (2010) 3947–3959, https://doi.org/10.1080/14786435.2010.502145.
[55] K. Schmuck, M. Burtscher, M. Alfreider, M. Wurmshuber, D. Kiener, Micro-mechanical fracture investigations on grain size tailored tungsten-copper nano-composites, JOM (2024), https://doi.org/10.1007/s11837-023-06348-7.
[56] M. Burtscher, et al., High-temperature nanoindentation of an advanced nano-crystalline W/Cu composite, Nanomaterials 11 (11) (2021) 1–13, https://doi.org/10.3390/nano11112951.
[57] M. Wurmshuber, S. Doppermann, S. Wurster, D. Kiener, Ultrafine-grained Tungsten by High-Pressure Torsion - Bulk precursor versus powder processing route, IOP Conf. Ser.: Mater. Sci. Eng. (2019), https://doi.org/10.1088/1757-899X/580/1/012051.
[58] T.G. Nieh, J. Wadsworth, Hall-petch relation in nanocrystalline solids, Scr. Metall. Mater. 25 (4) (1991) 955–958, https://doi.org/10.1016/0956-716X(91)90256-Z.
[59] A. Reuss, Berechnung der Fließgrenze von Mischkristallen auf Grund der Plastizitätsbedingung für Einkristalle, ZAMM - J. Appl. Math. Mech. / Zeitschrift Für Angew. Math. Und Mech. 9 (1) (1929) 49–58, https://doi.org/10.1002/zamm.19290090104.
[60] W. Voigt, Ueber die Beziehung zwischen den beiden Elasticitätsconstanten isotroper Körper [On the relationship between the two elastic constants of an isotropic body], Ann. Phys. 274 (12) (1889) 573–587.
[61] E. Lassner, W.-D. Schubert, Properties, chemistry, technology of the element, alloys, and chemical compounds, Kluwer Academic, 2005.
[62] F. Cardarelli, Materials Handbook. Springer (2018), https://doi.org/10.1007/978-3-319-38925-7.
[63] J.R. Davis, ASM Speciality Handbook, Copper and Copper Alloys. (2001).
[64] M.A. Meyers, A. Mishra, D.J. Benson, Mechanical properties of nanocrystalline materials, Prog. Mater. Sci. 51 (4) (May 2006) 427–556, https://doi.org/10.1016/j.pmatsci.2005.08.003.
[65] C. Suryanarayana, C.C. Koch, Nanocrystalline materials – Current research and future directions, Hyperfine Interact. 130 (1–4) (2000) 5–44, https://doi.org/10.1023/A:1011026900989.
[66] P. Chen, Q. Shen, G. Luo, M. Li, L. Zhang, The mechanical properties of W-Cu composite by activated sintering, Int. J. Refract. Met. Hard Mater. 36 (2013) 220–224, https://doi.org/10.1016/j.ijrmhm.2012.09.001.
[67] J.R. Trelewicz, C.A. Schuh, The Hall-Petch breakdown in nanocrystalline metals: a crossover to glass-like deformation, Acta Mater. 55 (17) (2007) 5948–5958, https://doi.org/10.1016/j.actamat.2007.07.020.
[68] H. Ryou, et al., Below the Hall-Petch Limit in Nanocrystalline Ceramics, ACS Nano 12 (4) (2018) 3083–3094, https://doi.org/10.1021/acsnano.7b07380.
[69] J. Gong, et al., Nano-metric self-diffusion of Fe: effect of grain size, RSC Adv. 7 (16) (2017) 9573–9578, https://doi.org/10.1039/c6ra28310a.
[70] A. Hohenwarter, R. Pippan, Fracture and fracture toughness of nanopolycrystalline metals produced by severe plastic deformation, Philos. Trans. R. Soc. A Math. Phys. Eng. Sci. 373 (2038) (2015), https://doi.org/10.1098/rsta.2014.0366.
[71] R. Pippan, A. Hohenwarter, The importance of fracture toughness in ultrafine and nanocrystalline bulk materials, Mater. Res. Lett. 4 (3) (2016) 127–136, https://doi.org/10.1080/21663831.2016.1166403.
[72] A. Pineau, A. Amine Benzerga, T. Pardoen, Failure of metals III: Fracture and fatigue of nanostructured metallic materials, Acta Mater. 107 (2016) 508–544, https://doi.org/10.1016/j.actamat.2015.07.049.
[73] M. Chandross, N. Argibay, Friction of metals: a review of microstructural evolution and nanoscale phenomena in shearing contacts, Tribol. Lett. 69 (4) (2021) 1–27, https://doi.org/10.1007/s11249-021-01477-z.
[74] J. C. M. Li, C. R. Feng, and B. B. Rath, "Emission of Dislocations from Grain Boundaries and Its Role in Nanomaterials," pp. 1–12, 2020, https://doi.org/10.3390/cryst11010041.
[75] D.N.F. Muche, M.A.T. Marple, S. Sen, R.H.R. Castro, Grain boundary energy, disordering energy and grain growth kinetics in nanocrystalline MgAl2O4 spinel, Acta Mater. 149 (2018) 302–311, https://doi.org/10.1016/j.actamat.2018.02.052.
[76] S. Zare Chavoshi, P.S. Branicio, Q. An, Transition between Hall-Petch and inverse Hall-Petch behavior in nanocrystalline silicon carbide, Phys. Rev. Mater. 5 (7) (2021) 1–11, https://doi.org/10.1103/PhysRevMaterials.5.073606.
[77] Y. Cao, et al., De-twinning via secondary twinning in face-centered cubic alloys, Mater. Sci. Eng. A 578 (2013) 110–114, https://doi.org/10.1016/j.msea.2013.04.075.
[78] P.J.L. Fernandes, D.R.H. Jones, The effects of microstructure on crack initiation in liquid-metal environments, Eng. Fail. Anal. 4 (3) (1997) 195–204, https://doi.org/10.1016/s1350-6307(97)00010-1.
[79] J.F. Ziegler, M.D. Ziegler, J.P. Biersack, SRIM - The stopping and range of ions in matter (2010), Nucl. Instrum. Methods Phys. Res. Sect. B Beam Interact. Mater. Atoms 268 (11–12) (2010) 1818–1823, https://doi.org/10.1016/j.nimb.2010.02.091.
[80] Kinchin, The displacement of atoms in solids during irradiation, Solid State Phys. 2 (1956) 307.
[81] B.T. McDermott, C.C. Koch, Preparation of beta brass by mechanical alloying of elemental copper and zinc, Scr. Metall. 20 (5) (1986) 669–672, https://doi.org/10.1016/0036-9748(86)90487-4.
[82] M. Burtscher, M. Alfreider, C. Kainz, D. Kiener, Deformation and failure behavior of nanocrystalline WCu, Mater. Sci. Eng. A 887 (August) (2023) 145760, https://doi.org/10.1016/j.msea.2023.145760.
[83] R. Bodlos, D. Scheiber, J. Spitaler, L. Romaner, Modification of the Cu/W Interface Cohesion by Segregation, Metals (Basel) 13 (2) (2023) 1–16, https://doi.org/10.3390/met13020346.
[84] J.M. Koo, H. Araki, S.B. Jung, Effect of Zn addition on mechanical properties of brass hollow spheres, Mater. Sci. Eng. A 483–484 (1–2 C) (2008) 254–257, https://doi.org/10.1016/j.msea.2006.01.183.
[85] I. Vishnevetsky, M. Epstein, Production of hydrogen from solar zinc in steam atmosphere, Int. J. Hydrogen Energy 32 (14) (2007) 2791–2802, https://doi.org/10.1016/j.ijhydene.2007.04.004.
[86] M. Schmid, "Vapor Pressure Calculator." Accessed: Apr. 15, 2024. [Online]. Available: https://www2.iap.tuwien.ac.at/www/surface/vapor_pressure.
[87] E. Harry, A. Rouzaud, P. Juliet, Y. Pauleau, M. Ignat, Failure and adhesion characterization of tungsten-carbon single layers, multilayered and graded coatings, Surf. Coatings Technol. 116–119 (1999) 172–175, https://doi.org/10.1016/S0257-8972(99)00071-7.
[88] E. Harry, A. Rouzaud, M. Ignat, P. Juliet, Mechanical properties of W and W(C) thin films: Young's modulus, fracture toughness and adhesion, Thin Solid Films 332 (1–2) (1998) 195–201, https://doi.org/10.1016/S0040-6090(98)01056-6.
[89] G. Dehm, J. Cairney, Implication of grain-boundary structure and chemistry on plasticity and failure, MRS Bull. 47 (8) (2022) 800–807, https://doi.org/10.1557/s43577-022-00378-3.
[90] M. Wurmshuber, M. Alfreider, S. Wurster, R. Pippan, D. Kiener, Small-scale fracture mechanical investigations on grain boundary doped ultrafine-grained tungsten, Acta Mater. 250 (118878) (2023) 18, https://doi.org/10.1016/j.actamat.2023.118878.
[91] J.D. Murphy, A. Giannattasio, Z. Yao, C.J.D. Hetherington, P.D. Nellist, S. G. Roberts, The mechanical properties of tungsten grown by chemical vapour deposition, J. Nucl. Mater. 386–388 (C) (2009) 583–586, https://doi.org/10.1016/j.jnucmat.2008.12.182.
[92] R.W. Margevicius, J. Riedle, P. Gumbsch, Fracture toughness of polycrystalline tungsten under mode I and mixed mode I/II loading, Mater. Sci. Eng. A 270 (2) (1999) 197–209, https://doi.org/10.1016/S0921-5093(99)00252-X.
[93] M.J. Pfeifenberger, V. Nikolić, S. Žák, A. Hohenwarter, R. Pippan, Evaluation of the intergranular crack growth resistance of ultrafine grained tungsten materials, Acta Mater. 176 (2019) 330–340, https://doi.org/10.1016/j.actamat.2019.06.051.
[94] J. Ast, M. Göken, K. Durst, Size-dependent fracture toughness of tungsten, Acta Mater. 138 (2017) 198–211, https://doi.org/10.1016/j.actamat.2017.07.030.
[95] M. Faleschini, H. Kreuzer, D. Kiener, and R. Pippan, "Fracture toughness investigations of tungsten alloys and SPD tungsten alloys," J. Nucl. Mater., vol. 367-370 A, no. SPEC. ISS., pp. 800–805, 2007, https://doi.org/10.1016/j.jnucmat.2007.03.079.
[96] E. Tejado, A.V. Müller, J.H. You, J.Y. Pastor, The thermo-mechanical behaviour of W-Cu metal matrix composites for fusion heat sink applications: The influence of the Cu content, J. Nucl. Mater. 498 (2018) 468–475, https://doi.org/10.1016/j.jnucmat.2017.08.020.
[97] E. Tejado, A.V. Müller, J.H. You, J.Y. Pastor, Mechanical behaviour of W particulate-reinforced Cu composites: Fracture toughness and R-curves, J. Nucl. Mater. 571 (2022), https://doi.org/10.1016/j.jnucmat.2022.153960.
[98] A. Giannattasio, S.G. Roberts, Strain-rate dependence of the brittle-to-ductile transition temperature in tungsten, Philos. Mag. 87 (17) (2007) 2589–2598, https://doi.org/10.1080/14786430701253197.
[99] D. Rupp, R. Mönig, P. Gruber, S.M. Weygand, "Fracture toughness and microstructural characterization of polycrystalline rolled tungsten", in International Journal of Refractory Metals and Hard Materials, Elsevier Ltd (2010) 669–673, https://doi.org/10.1016/j.ijrmhm.2010.05.006.